SCIENCE CHINA
Technological Sciences

• Article •

November 2017 Vol. 60 No. 11: 1658–1673
doi: 10.1007/s11431-016-9093-y

Flow reconstructions and aerodynamic shape optimization of turbomachinery blades by POD-based hybrid models

LUO JiaQi[1*], ZHU YaLu[1], TANG Xiao[1] & LIU Feng[1,2]

[1] *Department of Aeronautics and Astronautics, Peking University, Beijing 100871, China;*
[2] *Department of Mechanical and Aerospace Engineering, University of California, Irvine, CA 92697-3975, USA*

Received November 9, 2016; accepted July 5, 2017; published online September 26, 2017

This study presented a hybrid model method based on proper orthogonal decomposition (POD) for flow field reconstructions and aerodynamic design optimization. The POD basis modes have better description performance in a system space compared to the widely used semi-empirical basis functions because they are obtained through singular value decomposition of the system. Instead of the widely used linear regression, nonlinear regression methods are used in the function response of the coefficients of POD basis modes. Moreover, an adaptive Latin hypercube design method with improved space filling and correlation based on a multi-objective optimization approach was employed to supply the necessary samples. Prior to design optimization, the response performance of POD-based hybrid models was first investigated and validated through flow reconstructions of both single- and multiple blade rows. Then, an inverse design was performed to approach a given spanwise flow turning distribution at the outlet of a turbine blade by changing the spanwise stagger angle, based on the hybrid model method. Finally, the spanwise blade sweep of a transonic compressor rotor and the spanwise stagger angle of the stator blade of a single low-speed compressor stage were modified to reduce the flow losses with the constraints of mass flow rate, total pressure ratio, and outlet flow turning. The results are presented in detail, demonstrating the good response performance of POD-based hybrid models on missing data reconstructions and the effectiveness of POD-based hybrid model method in aerodynamic design optimization.

flow reconstruction, aerodynamic design optimization, proper orthogonal decomposition, turbomachinery, hybrid model, computational fluid dynamics, transonic

Citation: Luo J Q, Zhu Y L, Tang X, et al. Flow reconstructions and aerodynamic shape optimization of turbomachinery blades by POD-based hybrid models. Sci China Tech Sci, 2017, 60: 1658–1673, doi: 10.1007/s11431-016-9093-y

1 Introduction

With the increased power of computational speed, numerical simulation based on high-performance computers has become a useful tool in engineering. Usually, the mathematical model in a given discipline is first discretized to a system of algebraic equations with large dimensions. For example, to obtain the aerodynamic performance of airplanes and turbomachines, high resolution meshes with millions of grid points are necessary. The nonlinear partial differentiation governing flow equations are discretized and iteratively solved on each grid point until the computation converges. For aerospace applications involving tens of hundreds of flow computations, the computational time is unacceptable. Fortunately, model methods can be used to obtain approximate solutions with respect to the given inputs in a system space with much lower computational cost. For example, reduced-order models have been successfully applied in the disciplines of turbulence flow [1, 2] and aerodynamics [3–6].

At present, proper orthogonal decomposition (POD) has been successfully used to develop reduced-order models. The basis modes are the kernels of POD, which can be usually determined by singular value decomposition (SVD) of the sys-

---

*Corresponding author (email: jiaqil@pku.edu.cn)

tem ensemble. In such situations, the POD basis modes are self-adjustable for different system spaces. Compared to the widely used semi-empirical basis functions, such as polynomials and radial basis functions, POD basis modes are suggested to have a better response performance. It is known that usually only a series of primary basis modes cover a dominant part of the entire energy of a system, implying that a high-dimension problem in a system space can be described by a group of low-dimension models. In principle, any arbitrary vector in a system space can be described as a weighted summation form of primary basis modes. In the early applications, the determination of basis modes through SVD lacked sufficient accuracy and stability because of the large dimensions. To overcome these drawbacks, Sirovich [7] introduced the snapshot POD method, details of which have been introduced by the present authors [8]. Because of its high dimension reduction and robustness, snapshot POD is now widely used.

One important POD application is missing data reconstruction. On obtaining the basis modes of a system space, the missing data in incomplete vectors can be reconstructed by Gappy POD, which has been successfully applied in human-face characterization [9] and flow field reconstruction [10]. In the aerodynamics discipline, supposing a system space consisting of a number of different aerodynamic shapes is determined, the most intensive flow characteristics can be identified by the POD basis modes favoring the design and optimization to improve the aerodynamic performance. On the other hand, by regarding either the aerodynamic shape or the performance as the missing data of an incomplete vector, an inverse design or an optimization design can be accomplished by Gappy POD. Le Gresley and Alonso [11] introduced POD-based reduced-order models in their design optimization of airfoils. Bui-Thanh et al. [10] presented flow reconstructions by Gappy POD and achieved an inverse design of airfoils. Duan et al. [12] introduced a two-step design optimization based on Gappy POD and performed design optimization of airfoils. The applications of Gappy POD in turbomachinery were not studied until recent years [13–15].

In the missing data reconstruction based on Gappy POD, two crucial issues need to be taken into account, the number of primary basis modes and the sampling method. The number of basis modes used to describe a system space can significantly influence the description accuracy and the computational cost of missing data reconstruction. In early applications, Gappy POD with linear regression, such as the least-squares method, was widely used to obtain the coefficients of POD basis modes [10–12]. Unfortunately, the convergence history of description accuracy versus the number of basis modes performed zigzags, resulting in the difficulty on selecting the primary basis modes to describe a system space. In recent years, nonlinear regression, instead of linear regression methods, has been studied to improve not only the convergence performance but also the response accuracy of the coefficients of POD basis modes [14–16]. In the present study, two different nonlinear regression methods are introduced to construct the POD-based hybrid models.

Generally, one strives to obtain as few a number of snapshots as possible without deterioration in description accuracy by an appropriate sampling method. In recent years, rather than uniform sampling methods, some adaptive sampling methods were introduced in an attempt to reduce the sample number [14–19]. By these methods, the target subspace with the lowest description accuracy was determined first and then a number of additional uniform samples were added. In such situations, numerous samples were still required for a large number of inputs, which in reality exists in any adaptive experimental design based on uniform sampling. Due to its maximum space filling, the random sampling method Latin hypercube design (LHD) [20] has been widely used. At present, much work has been done to improve the LHD by taking into account space filling and correlation [21–25]. In the present study, an improved LHD based on multi-objective optimization was introduced to generate samples with maximin Euclidean distance and minimum correlation. Meanwhile, the adaptive sampling method based on the LHD was employed to reduce the total sample number. The performance of the improved LHD was illustrated and validated.

On obtaining the POD-based hybrid models with nonlinear regressions and improved LHD, flow reconstructions based on Gappy POD of three different turbomachinery blades, a supersonic steam turbine blade, a transonic compressor rotor, and a single low-speed compressor stage, were studied; and the performance of the POD-based hybrid models were compared to determine the appropriate hybrid model for design optimization. First, an inverse design approaching a given spanwise flow turning distribution by changing the spanwise stagger angle was performed to demonstrate the effectiveness of the POD-based hybrid model in design optimization. Then, the transonic compressor rotor blade, NASA Rotor 37, was redesigned through blade sweeping to improve the aerodynamic performance of shock loss, flow separation, and shock/tip-leakage interaction. Finally, the last stage of a 4.5-stage compressor was redesigned through stagger angle change along the span of the stator blade to reduce the flow separation zones around the suction surface and endwalls. The results are presented in detail and the influence of blade redesign on performance improvements are illustrated and discussed.

2 Proper orthogonal decomposition

2.1 Fundamentals

The principle and implementation of snapshot POD have already been introduced in ref. [8]. The crucial issues of snapshot POD are the determinations of eigenvalues and the corresponding eigenvectors of the autocorrelation matrix $\boldsymbol{R}$ through SVD.

$$\boldsymbol{R} = \frac{1}{n}(\boldsymbol{U}, \boldsymbol{U}) = \boldsymbol{Q}\left(\frac{1}{n}\boldsymbol{\Sigma}\boldsymbol{\Sigma}^{\mathrm{T}}\right)\boldsymbol{Q}^{\mathrm{T}}, \tag{1}$$

where $\boldsymbol{U}$ is the snapshot ensemble, which can be described in a decomposition form:

$$\boldsymbol{U} = \boldsymbol{Q}\boldsymbol{\Sigma}\boldsymbol{V}^{\mathrm{T}}, \tag{2}$$

where $\boldsymbol{Q}$ and $\boldsymbol{V}$ are the left and right orthogonal eigenmatrices, respectively, and Σ is a diagonal matrix containing all the eigenvalues. The eigenvectors, namely the basis modes of the snapshot ensemble $\boldsymbol{U}$, are

$$\boldsymbol{\Phi} = \{\psi_1, \psi_2, \cdots, \psi_n\} = \Sigma\boldsymbol{V}^{\mathrm{T}} = \boldsymbol{Q}^{\mathrm{T}}\boldsymbol{U}. \tag{3}$$

By snapshot POD, the autocorrelation matrix $\boldsymbol{R}$, rather than the snapshot ensemble $\boldsymbol{U}$, is decomposed. In the aerodynamics discipline, the dimension of $\boldsymbol{U}$ is inconceivable because of the high-resolution mesh. However, the dimension of $\boldsymbol{R}$ equals the number of snapshots, favoring the performance improvements of SVD. Once the basis modes are obtained, any arbitrary vector in a system space can be described in a weighted summation form as follows:

$$\boldsymbol{u} = \sum_{i=1}^{N} \lambda_i \psi_i + \varepsilon, \tag{4}$$

where N is the number of primary basis modes and $N \leqslant n$, λ_i are the corresponding coefficients, and ε denotes the reconstruction error, which can be determined by the deviation between the reconstructed and the exact solutions. Generally, in a given system space, the first several basis modes contain most of the intensive characteristics, favoring the description of the system space with sufficient accuracy by a reduced number of POD basis modes.

Gappy POD, an extension of snapshot POD, has been successfully used for the reconstructions of incomplete vectors [10–12, 15]. First, the complete and missing components in an incomplete vector are identified and placed into two subvectors distinguished by the subscripts “comp” and “miss”, respectively. Correspondingly, all the basis modes can be decomposed by two series of submodes. According to eq. (4), the subvector $\boldsymbol{u}_{\mathrm{comp}}$ can be described by

$$\mathbf{u}_{\mathrm{comp}} = \sum_{i=1}^{N} \lambda_i \psi_{i,\mathrm{comp}} + \varepsilon. \tag{5}$$

Since $\boldsymbol{u}_{\mathrm{comp}}$ and $\psi_{i,\mathrm{comp}}$ are known, the coefficient λ_i can be determined by the simple least-squares method. Then, the missing components can be filled up by

$$\boldsymbol{u}_{\mathrm{miss}} = \sum_{i=1}^{N} \lambda_i \psi_{i,\mathrm{miss}}. \tag{6}$$

The important capability of Gappy POD on missing data reconstruction contributes to POD applications in aerodynamic design optimization. Regarding the aerodynamic parameters as the “comp” subvector, an inverse design can be achieved by filling up the “miss” subvector (the aerodynamic shape). Similarly, optimization design can be achieved by regarding the aerodynamic shape as the “comp” subvector.

2.2 POD with nonlinear regression

Although by the least-squares method, the coefficients of POD basis modes can be successfully obtained in earlier research [10–12], however, there is still the potential to improve the description performance of Gappy POD on missing data reconstructions.

Since the least-squares regression belongs to one of the linear response methods, the present Gappy POD lacks sufficient description accuracy on missing data reconstructions in the intensive and discontinuous flow fields, such as the rotor tip-leakage flow and shock wave. It is imperative to improve the response accuracy of the coefficients of POD basis modes. In recent years, to supply the coefficients of POD basis modes, nonlinear regression instead of the least-squares method has been studied [14–16]. One simple but robust technique is surrogate model response.

It is well known from eq. (2) that the snapshot ensemble can be exactly described by the basis modes.

$$\boldsymbol{U} = \boldsymbol{Q}\boldsymbol{\Phi}. \tag{7}$$

Eq. (7) implies that by regarding each snapshot as a model input, one column of the coefficient matrix $\boldsymbol{Q}$ can be specified as the corresponding function. In such cases, with n given snapshots, N different surrogate models with respect to the N primary basis modes can be constructed in the general formula

$$\boldsymbol{q}_i = \sum_{k=1}^{p} \beta_{ik} \boldsymbol{f}_k(\boldsymbol{x}) + \varepsilon_m, \quad i = 1, \cdots, N, \tag{8}$$

where $\boldsymbol{q}_i$ denotes the i-th column, $\boldsymbol{f}_k$ is the k-th basis function of the surrogate model, $\boldsymbol{x}$ is the input vector, and β_{ik} are the model variables required to be determined.

In a previous study [15], the radial basis function (RBF) [26] response method was used to determine the coefficients of POD basis modes. By the nonlinear regression method, the convergence of response deviation versus the number of basis modes performed much better than the linear-regression-based Gappy POD. Meanwhile, the description accuracy of the POD-RBF hybrid model was significantly improved, even for transonic flow reconstructions. It is widely recognized that the function response by the RBF model performs much better for strong nonlinear problems, whereas its superiority is not so distinct in the weak nonlinear and linear problems. In the present study, flow reconstructions by Gappy POD were performed for a supersonic turbine stator, a transonic compressor rotor, and a low-speed compressor stage involving complex and typical flows. In such cases, the quadratic polynomials and RBF were employed to construct the response surfaces, the performances of which are compared in the following sections. The quadratic polynomial response surface (QPRS) and Gauss's radial basis function are given by eqs. (9) and (10), respectively.

$$y = \xi_0 + \sum_{i=1}^{n} \xi_{ii} x_i x_i + \sum_{i=1}^{n-1} \sum_{j=i+1}^{n} \xi_{ij} x_i x_j, \tag{9}$$

$$\phi(r) = e^{-cr^2}, \quad r_{ij} = \|\boldsymbol{x}_i - \boldsymbol{x}_j\|_2, \tag{10}$$

where c is the model parameter, and r_{ij} is the Euclidean distance between the i-th and j-th snapshots. Using the QPRS method, the model variables can be obtained by the least-squares method. Nevertheless, by using the RBF, the exact solutions of the model variables can be determined by solving a system of linear equations.

Once the surrogate models are obtained, the coefficients corresponding to an arbitrary vector regarded as the model input can be quickly responded. Consequently, the missing data reconstruction can be accomplished following eq. (6).

3 Descriptions of design optimization

3.1 Cost function

In the present study, an inverse design is firstly studied based on Gappy POD to validate the effectiveness and accuracy of the POD-based hybrid models. A supersonic steam turbine stator blade is redesigned by changing the spanwise stagger angle to approach a given spanwise distribution of outlet flow turning. The cost function is given as

$$I = \frac{1}{2} \int_r [\beta(r) - \beta_0(r)]^2 \, \mathrm{d}r, \tag{11}$$

where $\beta(r)$ denotes the circumferentially mass-averaged flow turning along span, the subscript 0 represents the target. The flow turning is defined as the arc tangent of the ratio of circumferential velocity to the axial velocity.

In turbomachinery studies, flow loss is a parameter that can be measured by either entropy production at the outlet [27] or by adiabatic efficiency. The present design optimizations of a transonic compressor rotor and a single compressor stage were investigated to improve the adiabatic efficiency given as

$$I = \eta = \frac{\pi^{(\gamma-1)/\gamma} - 1}{\theta - 1}, \tag{12}$$

where η denotes the adiabatic efficiency, π and θ denote the ratios of total pressure and total temperature at the outlet to those at the inlet, respectively, and γ is the specific heat ratio.

Generally, the operation condition of compressor rotors can be described by parameters including rotation speed, total pressure ratio, and mass flow rate. In the optimization, the operation condition is not allowed to be changed. In other words, optimization is performed with a fixed rotation speed, while the total pressure ratio and mass flow rate are required to be maintained. For the last stage of the multi-stage compressor, to adjust to the inlet flow of the downstream experiment section, the outlet flow is not allowed to deviate significantly from the designed flow. In such cases, the optimization constraints are given as

$$\Delta\dot{m} = 1 - \frac{\dot{m}}{\dot{m}_0} \leqslant \epsilon_1, \quad \Delta\pi = 1 - \frac{\pi}{\pi_0} \leqslant \epsilon_2, \tag{13}$$

for the optimization of the transonic rotor blade, and

$$\Delta\beta = 1 - \frac{\beta}{\beta_0} \leqslant \epsilon_3, \tag{14}$$

for the optimization of the single stage. $\dot{m}_0, \pi_0, \beta_0$ are the references, and ϵ_1, ϵ_2, ϵ_3 are the change tolerances of mass flow rate, total pressure ratio, and flow turning, respectively.

3.2 Parametrization

NASA Rotor 37, designed and experimentally investigated by the NASA Lewis Research Center in the 1970s [28], is a single rotor blade row. The flow through transonic compressor rotors exhibit many intensive flow features, including the shock perpendicular to the casing, tip-leakage flow, and shock-leakage interaction. In previous work [29], it was found that by modifying the aerodynamic shape of transonic rotors, the shock loss and the detrimental effects of shock-leakage interaction can be reduced. However, since the shock cannot be moved on the compressor casing, the improvements on shock-leakage interaction were quite limited. The design of blade sweep and lean has been proved to be useful to move the relative position of the shock. Not only the flow loss but also the flow diffusion in the tip gap induced by the shock-leakage interaction can be reduced [30, 31]. Figure 1 illustrates the upward sweeping of Rotor 37, where Δx denotes the axial displacement of the leading edge. It should

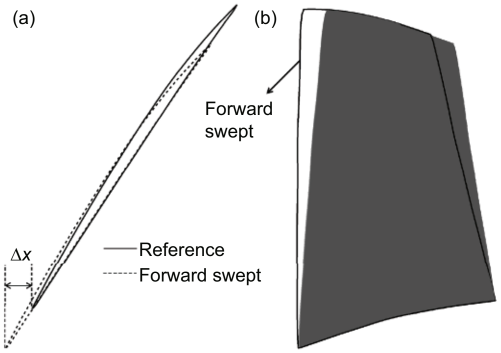

Figure 1 Sketch of sweeping. (a) Top view; (b) side view.

be noted that, by the present sweep technology, the blade is moved along the actual chord direction to avoid the effects of blade sweeping on the structure performance [30].

Figure 2 presents the 4.5-stage low-speed research compressor designed for a wind tunnel [32]. For the linear stator blade, flow separation zones in the corners of the suction side and the endwalls exist, resulting in most of the flow losses. In the optimization, the stagger angle of only the stator blade of the last stage was redesigned, while the rotor blade was unchanged to maintain the structure performance.

The stagger angle change was achieved by a parameterization method presented in previous work [29], by which the redesigned blade due to spanwise stagger change was configurated first by projecting a two-dimensional blade profile onto an auxiliary plane to maintain the rigid rotation, then the updated blade profile was recovered from the corresponding rotated profile on the auxiliary plane. Considering the ease of manufacturing the spanwise stagger angle and blade sweep, the multiphase quadratic polynomial parameterization method as shown by eq. (15) was employed.

$$\alpha_r = \alpha_{i-1} + \frac{(r - r_{i-1})^2}{(r_i - r_{i-1})^2}(\alpha_i - \alpha_{i-1}), \quad r_{i-1} < r \leqslant r_i, \tag{15}$$

where r_i are the selected spans from hub to the casing and r_0 corresponds to the hub, α_r denotes the spanwise distribution of either the stagger angle change or the sweep, and α_i are the corresponding design parameters. By this parameterization method, the spanwise stagger angle change and blade sweep can be determined, and then the perturbed aerodynamic shape can be configurated.

3.3 Flow solver

An in-house program entitled Turbo90 [33, 34] was used to obtain the flow solutions in our study. A one-equation turbulence model [35] was employed to resolve the eddy viscosity. At present, the program has already successfully predicted the aerodynamic performance of both turbine and compressor blades [29, 36–38].

To achieve the flow computations of multiple blade rows with reduced computational efforts, mixing-plane methods [39–41] are usually used to make the unsteady flow computations to quasi-steady ones. The mixed-out method [41] was employed in this study because of its strong conservation of convective fluxes. The implementation of the mixed-out method is briefly introduced in the following.

First, the integrals of convective fluxes had to be obtained on both the upstream and downstream sides of the interface.

$$\begin{cases} F_1 = \int_A \rho \boldsymbol{U} \cdot \mathrm{d}\boldsymbol{A} & = \bar{\rho}\bar{U}, \\ F_2 = \int_A (\rho u \boldsymbol{U} + p\boldsymbol{n}) \cdot \mathrm{d}\boldsymbol{A} & = \bar{\rho}\bar{u}\bar{U} + \bar{p}\bar{S}_x, \\ F_3 = \int_A (\rho v \boldsymbol{U} + p\boldsymbol{n}) \cdot \mathrm{d}\boldsymbol{A} & = \bar{\rho}\bar{v}\bar{U} + \bar{p}\bar{S}_y, \\ F_4 = \int_A (\rho w \boldsymbol{U} + p\boldsymbol{n}) \cdot \mathrm{d}\boldsymbol{A} & = \bar{\rho}\bar{w}\bar{U} + \bar{p}\bar{S}_z, \\ F_5 = \int_A \rho H \boldsymbol{U} \cdot \mathrm{d}\boldsymbol{A} & = \bar{\rho}\bar{H}\bar{U}, \end{cases} \tag{16}$$

where $\{\rho, u, v, w, p\}$ are the primitive variables, $\boldsymbol{U}$ and $\mathrm{d}\boldsymbol{A}$ are the vectors of velocity and area, respectively, and $\boldsymbol{n}$ is the unit normal vector, and

$$\bar{U} = \bar{u}\bar{S}_x + \bar{v}\bar{S}_y + \bar{w}\bar{S}_z.$$

The variables with the top symbol bar are the averages. However, $\bar{S}$ is the area summation of all the circumferential cells on each span. Additionally, the total enthalpy is involved to close the system of equations.

$$H = \frac{\gamma}{\gamma - 1}\frac{p}{\rho} + \frac{1}{2}U^2.$$

Finally, the average pressure can be determined as

$$\bar{p} = \frac{1}{\gamma + 1}\left[\frac{a}{b} \pm \sqrt{(a/b)^2 + (\gamma^2 - 1)(c - 2F_1F_5)/b}\right], \tag{17}$$

Figure 2 Sketch of the multi-stage compressor.

where

$$a = F_2\bar{S}_x+F_3\bar{S}_y+F_4\bar{S}_z,\ \ b = \bar{S}_x^2+\bar{S}_y^2+\bar{S}_z^2,\ \ c = F_2^2+F_3^2+F_4^2.$$

As mentioned in eq. (17), the positive sign before the square root corresponds to subsonic flow, while the negative sign corresponds to supersonic flow.

Once the average pressure is obtained, the averages of other flow variables can be determined. Then, the exchange of flow variables between the adjacent blade rows, i.e., between the upstream and downstream sides of the interface, must be performed. Non-reflective boundary conditions based on one-dimensional characteristic equations were implemented.

Before performing POD-based design optimization, the in-house program was employed to obtain the grid-independent solutions for NASA Rotor 37 and the last stage of the 4.5-stage compressor. For each validation case, three meshes with different resolutions were tested. The grid number in the streamwise direction was maintained and those in the circumferential and spanwise directions were doubled. At the operation condition near peak efficiency of Rotor 37, the computed mass flow rate, total pressure ratio and adiabatic efficiency of Grid 1 and Grid 2 were significantly different, whereas the solutions of Grid 2 and Grid 3 were similar (Table 1). Hereby, Grid 2 was employed in the following design optimization study.

Figure 3 presents comparisons between the experimental and CFD flow solutions along the span. Generally, the total pressure ratio of CFD matched well with the experimental results, while the deviation of total temperature ratio on the spans from 50% to 80% blade height was evident, resulting in a drop of CFD-based adiabatic efficiency on the corresponding spans. The aerodynamic performance of the entire operation range is compared to the experimental results in Figure 15. In the CFD operation range, the characteristics of total pressure ratio were close to experimental values. However, as shown in Figure 3, the CFD-based adiabatic efficiency was dramatically low, as a result of the over-prediction of total temperature ratio.

The 4.5-stage compressor designed by the present group for research [32] had no experimental results for CFD validation. However, by using the in-house program, grid-independent solutions were obtained, as shown in Table 2. The flow solutions of the grids with the “suffix stator” are those for the last stage, rather than those of the single stator. Similar to Table 1, the results in Table 2 demonstrate excellent grid convergence. Grid 2 was employed in the following design optimization study.

4 Design of experiments

4.1 Adaptive LHD by optimization

Uniform sampling methods are used in many model studies [10–12, 31]; however, the main drawback is that the number of necessary samples exponentially increases with an increase in input numbers. LHD, by the random sampling technique, has been widely used because of its full-space filling with fewer samples. In the past two decades, much work on LHD computer experiments has been reported [21–25]. Ye

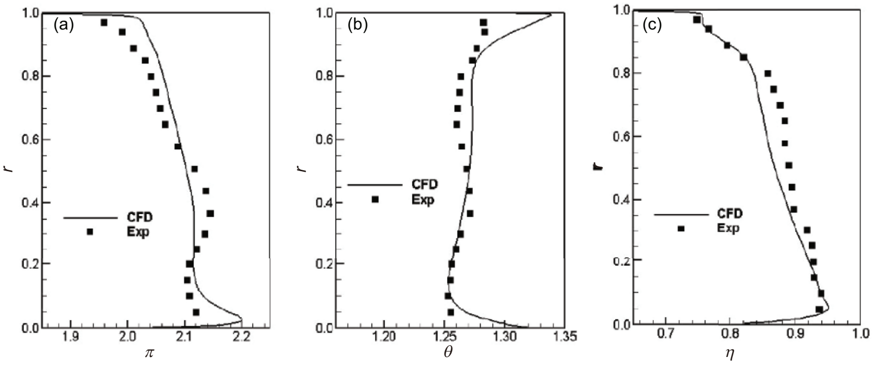

Figure 3 Comparisons of spanwise flow distributions of Rotor 37. (a) Total pressure ratio; (b) total temperature ratio; (c) adiabatic efficiency.

Table 1 Grid-independent flow solutions of Rotor 37

Grid	Resolution	$\dot{m}$	π	η
Grid 1	121 × 25 × 33	0.9915	2.0842	0.8753
Grid 2	121 × 49 × 65	0.9935	2.0828	0.8728
Grid 3	121 × 97 × 129	0.9941	2.0822	0.8719

Table 2 Grid-independent flow solutions of the last stage

Grid	Resolution	$\dot{m}$	π	η
Grid 1_rotor	105 × 25 × 25	0.9112	1.0657	0.9620
Grid 2_rotor	105 × 49 × 49	0.9090	1.0638	0.9589
Grid 3_rotor	105 × 97 × 97	0.9085	1.0631	0.9577
Grid 1_stator	113 × 25 × 33	0.9105	1.0634	0.9141
Grid 2_stator	113 × 49 × 65	0.9089	1.0616	0.9120
Grid 3_stator	113 × 97 × 129	0.9085	1.0611	0.9113

[22] proposed an orthogonal LHD (OLHD), by which the correlation of an arbitrary sample pair was exactly zero, whereas the sample number was strictly dependent on the number of inputs. To relieve the undesirable dependence, Joseph and Hung [25] employed a multi-objective optimization approach to pick up LHD samples from a design space.

Although the aforementioned LHD methods can supply improved samples, they are essentially one kind of static sampling method, where the function response is not taken into account in the model construction. Following the adaptive sampling method introduced in previous work [15], in the present study, an adaptive LHD method based on multi-objective optimization was implemented as follows.

Step 1: Obtain LHD training samples and test samples, then construct the POD hybrid model based on the training samples.

Step 2: Obtain the function response and the corresponding response deviation of each test sample.

Step 3: Quit the procedure if the averaged deviation falls below the tolerance, or else specify the target subspace and go to **Step 4**.

Step 4: Add a number of additional LHD samples into the target subspace to update the hybrid model, go to **Step 2**.

After obtaining the LHD samples of **Step 1** and **Step 4**, the multi-objective optimization with the correlation and Euclidean distance selected as the objectives is performed.

$$\text{Min.}\ \lambda\bar{\rho}_c + (1-\lambda)\bar{D}, \tag{18}$$

where λ denotes the weight (λ=0.5), $\bar{\rho}_c$ and $\bar{D}$ are the average correlation coefficient and average maximin Euclidean distance, respectively, the definitions of which are given as

$$\bar{\rho}_c = \frac{2}{n(n-1)} \sum_{i=1}^{n-1} \sum_{j=i+1}^{n} \frac{(\boldsymbol{u}_i - \bar{u}_i)(\boldsymbol{u}_j - \bar{u}_j)}{\|\boldsymbol{u}_i - \bar{u}_i\|\|\boldsymbol{u}_j - \bar{u}_j\|}, \tag{19}$$

$$\bar{D} = \frac{2}{n(n-1)} \sum_{i=1}^{n-1} \sum_{j=i+1}^{n} \frac{1}{\|\boldsymbol{u}_i - \boldsymbol{u}_j\|_2}. \tag{20}$$

Starting from a sequential permutation $\{1, \cdots, n-1, n\}^{\mathrm{T}}$, a computer-aided random sampling procedure was employed to achieve data exchange for each element of the permutation. After a complete exchange process, a perturbed permutation was obtained. Ultimately, among a group of permutations, the multi-objective optimization was achieved by a simple searching method.

Finally, with the aforementioned techniques, the process of the POD-based hybrid model construction is illustrated in Figure 4, where Module I supplies the test samples used for the response validation of the POD-based hybrid models. The uniform sampling method was employed to evenly cut the full system space into a series of subspaces, each of which is responded by the POD-based models. Module II strives to generate the additional LHD samples added into the target subspace.

4.2 Illustrations and validations

To evaluate the effectiveness of the adaptive LHD (ALHD) developed in the present study, the function response of aerodynamic parameters by the POD-based hybrid models was investigated. Shape snapshots were obtained by perturbing the blade sweep of NASA Rotor 37. For the ease of illustration, only two control points at the middle span and blade tip were selected. A number of 5^2 uniform samples regarded as

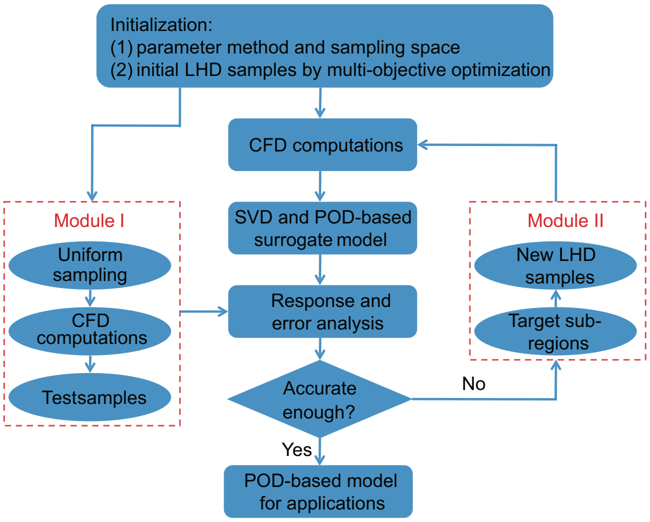

Figure 4 (Color online) Process map of POD-based surrogate model construction by LHD.

test samples were generated in the design space, cutting the entire design space into 25 even subspaces. An initial LHD with 21 samples was obtained by multi-objective optimization. Through a model response of each test sample, the average response deviation was calculated by

$$\bar{\varepsilon} = \sqrt{\frac{1}{m}\sum_{i=1}^{m}\left(\frac{f_{i,\mathrm{POD}} - f_{i,\mathrm{CFD}}}{f_{i,\mathrm{CFD}}}\right)^2}, \tag{21}$$

where f denotes the aerodynamic parameter of interest, m is the number of test samples, and the subscripts "POD" and "CFD" represent the model responded and computed solutions, respectively. The adiabatic efficiency at the outlet of Rotor 37 was responded and the deviation tolerance was 0.01.

Once the target subspace was specified in each ALHD cycle, four additional samples were added. The updated ALHD sample ensemble including all the additional and initial samples should be the optimal of the multi-objective optimization in the current ALHD cycle. Furthermore, all the samples determined in the current ALHD cycle were fixed in the following ALHD cycles. In such cases, only four additional flow computations were necessary in each ALHD cycle. Figure 5 illustrates the ALHD samples in the design space. After only two ALHD cycles, the average response deviation of the POD-RBF model fell below tolerance. Ultimately, the sample number for the POD-RBF model was 29, while it was 33 for the POD-QPRS model.

To demonstrate the improvements of ALHD on model construction efficiency, another LHD method referred to as static LHD method (SLHD) was also studied. The samples of the SLHD method were determined by only the initial multi-objective optimization. Figure 6 presents the convergence history of the average response deviation versus the sample number. It is well known that the numbers of necessary samples based on ALHD for constructing POD-based hybrid models are significantly reduced compared with those of SLHD because the sensitive subspaces can be specified by ALHD, where the additional samples are added favoring the improvements of overall response accuracy. Nevertheless, the sensitive subspaces are not taken into account by SLHD, resulting in a waste of samples in the non-sensitive subspaces; this is proved by Figure 5. There are more ALHD samples in the subspaces of a large blade sweep at both middle span and blade tip. Generally, compared with the POD-QPRS model, the response performance of the POD-RBF model was better for this test case.

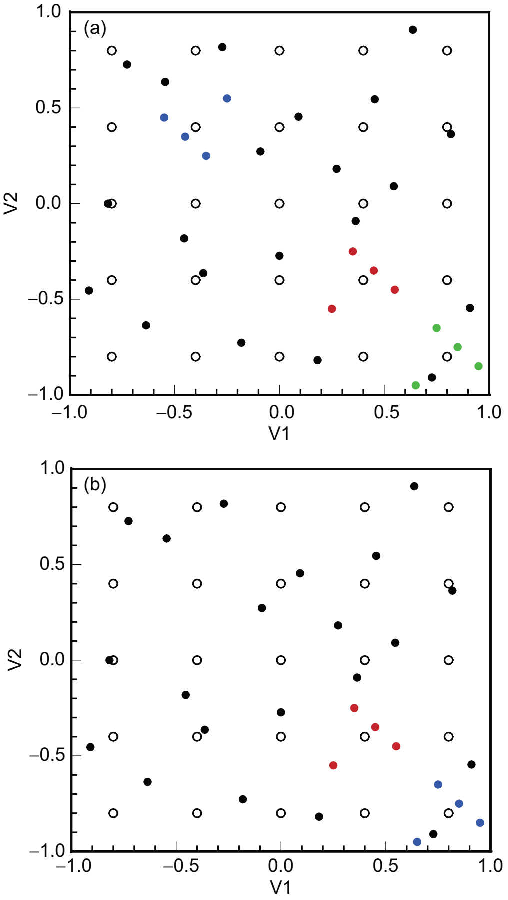

Figure 5 (Color online) ALHD samples in the design space. (a) POD-QPRS; (b) POD-RBF.

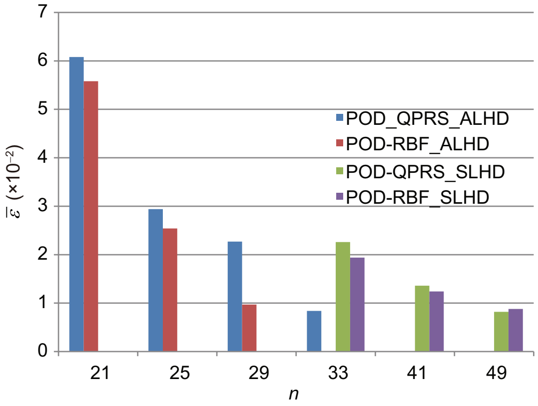

Figure 6 (Color online) Histograms of convergence history of the average deviation versus the sample number.

5 Design optimization

Three different optimization cases were investigated, an inverse design to approach a given flow turning distribution, and redesigns of a transonic compressor rotor blade and a single compressor stage to improve adiabatic efficiency. The response performance of the POD-QPRS and POD-RBF hybrid models were validated first, followed by the optimization studies. A genetic algorithm (GA) was employed to determine the optimal starting from 50 individuals. The aerodynamic parameters of each individual were obtained by model response.

5.1 Flow turning inverse design

5.1.1 Model validation

In the inverse design through stagger angle change along the span, five control points were uniformly distributed on 0%, 25%, 50%, 75%, and 100% spans of a supersonic turbine blade, the geometric model of which is illustrated in Figure 7. With a given input of stagger angle change on the five control spans, the spanwise stagger angle change was determined by using the polynomial parametrization method, as shown in eq. (15). The sample turbine blade was then configurated by the introduced parametrization method [29]. Once the flow solutions were obtained, the spanwise distributions of stagger angle change and the outlet flow turning were regarded as one POD snapshot. Once the ensemble was obtained, the POD basis modes were determined by SVD and ultimately used for the reconstructions of the spanwise flow.

The difference between the designed and target spanwise flow turning distributions as shown in eq. (11) is responded. The allowance of maximum average deviation as shown in eq. (21) was 0.1. Thirty-two uniform samples were generated in the design space to be used as test samples. By using the proposed ALHD, starting from 49 initial LHD samples, two groups of training samples were ultimately obtained for constructing the POD-QPRS and POD-RBF hybrid models. Table 3 presents the sample numbers and the average deviations between the CFD and the responded flow turning distributions. It can be seen from Table 3 that by using the RBF model to respond the coefficients of the POD basis modes, fewer samples were necessary to obtain the equivalent response accuracy. For the inverse design, the POD-RBF model and the corresponding group of training samples were used.

Figure 8 compares the spanwise flow turning distributions obtained from the CFD and the POD-RBF model for the reference blade and the test samples with a uniform negative and positive stagger angle change of one degree. With given spanwise stagger angle changes, the POD-RBF hybrid model successfully reconstructed the corresponding flow turning distributions along the span with excellent accuracy.

5.1.2 Inverse design

The inverse design was performed based on the POD-RBF hybrid model. By using GA, each individual contained the stagger angle change at five control spans. Once the spanwise stagger angle change of each individual was obtained by using the polynomial parametrization method, the corresponding flow turning distribution regarded as the missing subvector was reconstructed by the POD-RBF model; then the cost function as shown in eq. (11) was calculated.

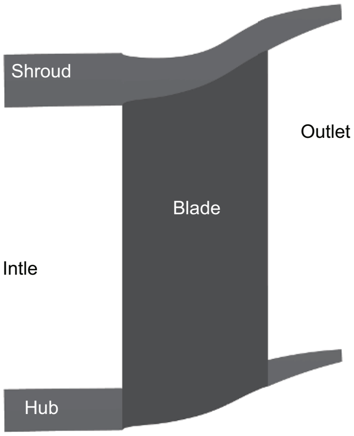

Figure 7 Geometric sketch of steam turbine blade.

Table 3 Sample numbers and average deviations of flow turning

Model	n	$\bar{\epsilon}$
POD-QPRS	113	8.58×10^{-2}
POD-RBF	89	9.17×10^{-2}

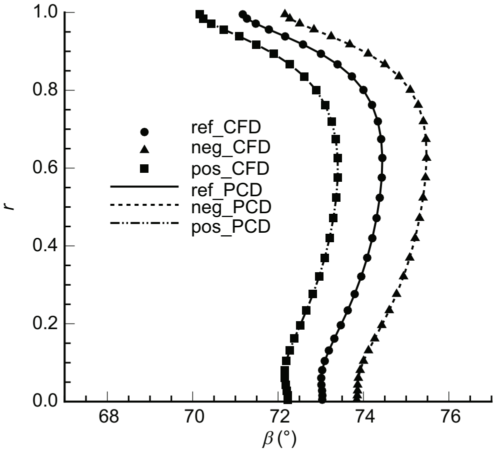

Figure 8 CFD and POD solutions of spanwise flow turning.

Figure 9 presents the optimal spanwise distribution of stagger angle change. Figure 10 compares the spanwise flow turning distributions of the target and those of the reference and optimized blades, where the suffix “CFD” indicates the flow turning obtained from CFD. From these pictures, it can be seen that the stagger angle performed negative changes when the target flow turning was larger than the reference and vice versa. Both the model-responded and CFD-based spanwise flow turning distributions of the optimized blade were very close to the target. Furthermore, the model-responded

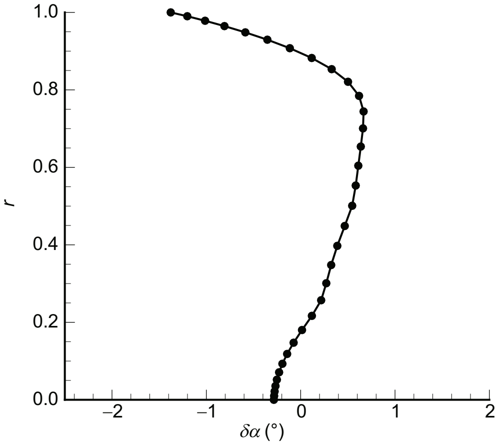

Figure 9 Spanwise distribution of stagger angle change.

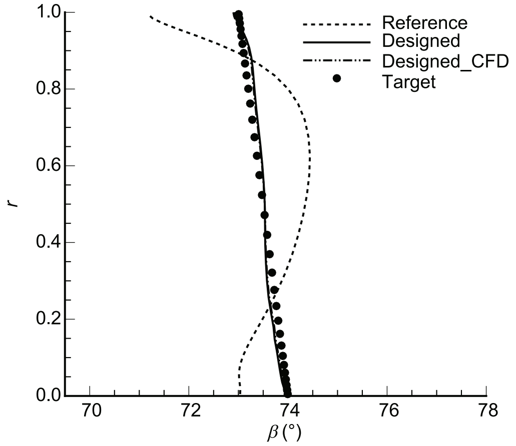

Figure 10 Spanwise distributions of flow turning.

flow turning distribution was almost a duplicate of the CFD one, further demonstrating the sufficient response accuracy of the POD-RBF hybrid model.

The results of the flow turning inverse design demonstrated that the POD-based hybrid model not only accurately reconstructed the missing flow field as a reduced-order model, but also accomplished the design optimization as a surrogate model coupled with an optimization method.

5.2 Blade sweeping of compressor rotor

5.2.1 Model validation

In the present study, four control points located on 33.3%, 66.7%, 90%, and 100% spans were perturbed in the actual chord direction of NASA Rotor 37. With a given input of blade sweep on the four spans, the spanwise blade sweep can be determined by eq. (15). However, the blade sweep was determined by the axial displacement as shown by Figure 1. Once the flow solutions were computed, the spanwise distributions of blade sweep and outlet flow were regarded as one POD snapshot.

A group of 3^4=81 samples was placed in the design space as test samples. A second group of 31 multi-objective optimized samples was selected and used as initial LHD samples. Adiabatic efficiency, mass flow rate, and total pressure ratio at the operation condition near peak efficiency of Rotor 37 needed to be responded. The tolerance of the maximum average deviation among the three aerodynamic parameters was 0.01. By using the introduced ALHD method, the maximum average deviation of the POD-RBF model with 67 samples was below the tolerance. Table 4 presents the sample numbers for reconstructing the POD-QPRS and POD-RBF hybrid models and the corresponding average deviations. It can be seen that among the three aerodynamic parameters, the function response of adiabatic efficiency demonstrated the slowest convergence. The average deviation of the mass flow rate of POD-RBF model was a little higher than that of the POD-QPRS model. In the following design optimization, the POD-RBF model and the corresponding group of ALHD samples were used.

Figure 11 presents the pressure contours of the reference Rotor 37 on the blade-to-blade streamsurface at the blade tip with two different back pressures, $p1$ and $p2$. In fact, $p1$ and $p2$ correspond to the operation conditions of Rotor 37 near the peak efficiency and near stall, respectively, which are illustrated in Figure 15. As pointed out in previous work [15], besides the suction flow, more intensive flow characteristics exist in the tip gap of transonic compressor rotors, resulting in more samples and lower description accuracy on the flow reconstructions based on the POD-RBF hybrid model. In the present study, by using the ALHD method, only 67 samples were necessary and the reconstructed flow fields in the tip gap were almost duplicates of those obtained from CFD, demonstrating the convincing response performance of the current POD-RBF model.

5.2.2 Optimization design

With respect to each GA individual, once the corresponding

Table 4 Sample numbers and average deviations

Model	n	$\bar{\epsilon}_\eta$	$\bar{\epsilon}_\pi$	$\bar{\epsilon}_{\dot{m}}$
POD-QPRS	75	9.79×10^{-3}	4.27×10^{-3}	3.24×10^{-4}
POD-RBF	67	8.73×10^{-3}	3.29×10^{-3}	3.46×10^{-4}

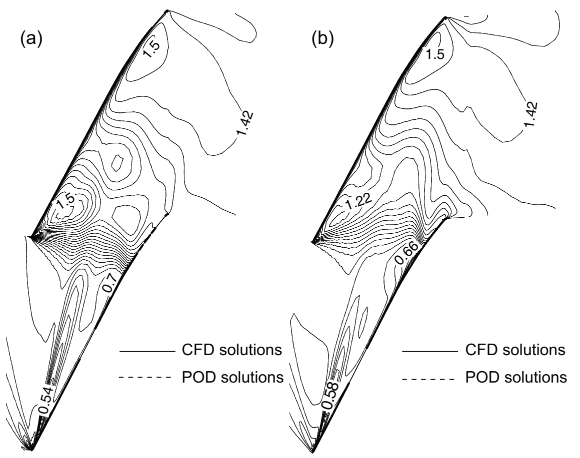

Figure 11 Pressure contours on the blade-to-blade streamsurface at the blade tip. (a) $p2$; (b) $p1$.

spanwise distribution of blade sweep was obtained by eq. (15), the mass flow rate, circumferentially mass-averaged total pressure ratio, and adiabatic efficiency along the span regarded as the missing subvectors were obtained by the POD-RBF model, based on which the overall performance parameters can be determined. Then, the cost function given by eq. (12) was calculated. To maintain the operation condition of NASA Rotor 37, the mass flow rate and total pressure ratio were regarded as constrains in the design optimization with change tolerances $\epsilon_1 = \epsilon_2 = 0.5\%$.

An optimal swept blade was ultimately determined with a gain of 0.73% for adiabatic efficiency, while the deviations of mass flow rate and total pressure ratio were 0.12% and 0.46%, respectively, demonstrating the enforced optimization constrains. Figure 12 presents the relative displacement of the blade in the axial chord direction, where c_h denotes the axial chord on the hub. The spanwise distribution of total pressure ratio and adiabatic efficiency at the outlet of both reference and optimized blades are also given. From the hub to the 70% span, the blade is back swept, while it is forward swept from the 70% span to the blade tip. The change of the spanwise sweep resulted in a redistribution of loading along the spanwise direction: the loading on the tip region was reduced, and that in the mid-span region increased, thus leading to an efficiency gain near the tip while an efficiency drop near the mid-span, as shown in Figure 12. The total pressure ratio increased from about 40% to 80% spans and decreased on the others, resulting in a maintained optimization constraint.

As previously mentioned, the sweep optimization of transonic rotor blades strive to move the relative position of shock on the casing. Figure 13 presents the isentropic relative Mach number distributions on 10%, 50% and 90% spans of the reference and optimized blades. On the 10% and 90% spans, the shock moved downward, contributing to adiabatic efficiency improvements. However, the shock moved upward on the 50% span and the adiabatic efficiency slightly decreased.

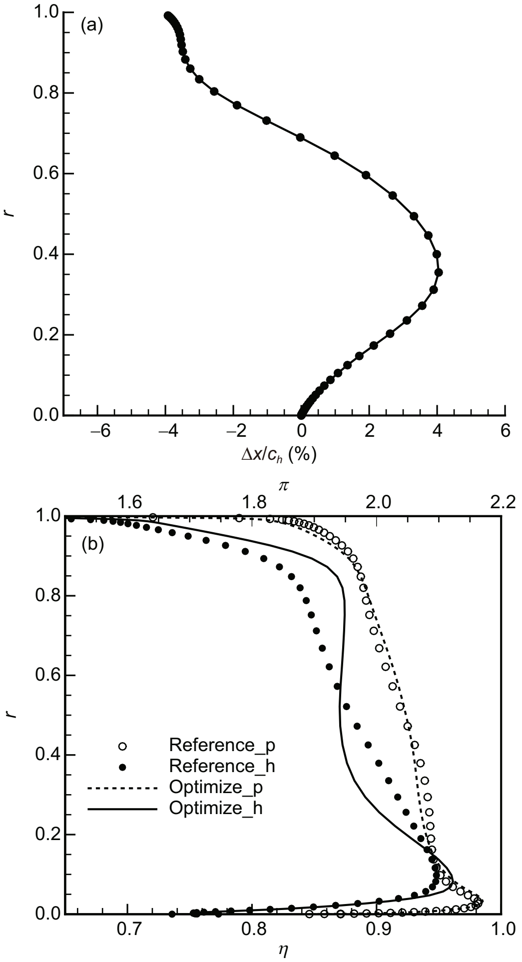

Figure 12 Spanwise distributions. (a) Sweep; (b) total pressure ratio and adiabatic efficiency.

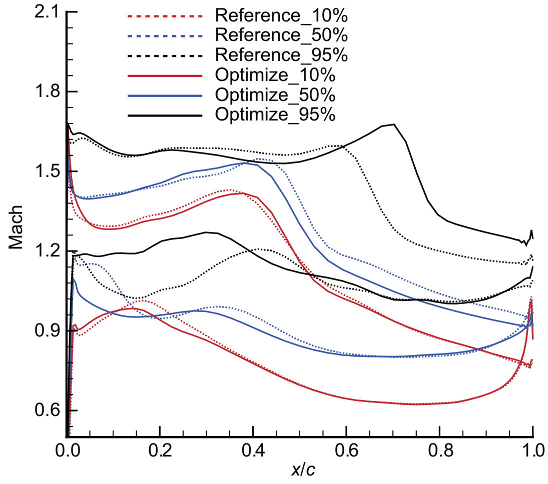

Figure 13 (Color online) Isentropic relative Mach number on three different spans.

To illustrate the details of performance improvements, the contours of isentropic relative Mach number near the suction side are presented in Figure 14. It is well known that for high-compression-ratio transonic rotors, the interaction between shock waves and leakage flow near the blade tip is regarded as one main stall [36]. Through sweep optimization, the downward moving shock on the blade tip and the resultant weakened shock/tip-leakage interaction favored improving the stability of transonic compressor rotors [30, 31]. The operation characteristics of the reference and optimized rotor blades are compared in Figure 15.

It can be seen from Figure 15 that in the entire operation range, the improvement of adiabatic efficiency was significant. Moreover, the rotor stalled at about 97.5% choke mass flow rate compared to 93% in experiment [28]. Although the stall point cannot be accurately resolved by steady CFD codes, some simple but widely used means can be employed to evaluate rotor stall. As pointed out in previous work [36], the decrement ratio of mass flow rate against a fixed back pressure increment and the flow diffusion in the tip gap induced by shock/tip-leakage interaction can be used. In Figure 15, obviously, the stall mass flow rate was much lower after sweep optimization, demonstrating the improved stall margin. Figure 16 presents the contours of relative Mach number on the blade-to-blade streamsurface at the blade tip. The symbols “S.F.”, “L.V.”, and “S.S.” represent shock front, leakage vortex, and suction shock, respectively. As the back pressure increased, the suction shock moved upward. After sweep optimization, the shock moved downward significantly compared to the references; furthermore, the origins of tip-leakage vortex moved slightly downward. All the aforementioned improvements favor the reduction of shock/tip-leakage interaction. Moreover, as shown in Figure 16, the regions with low relative Mach number, namely intensive flow diffusion, were significantly reduced, demonstrating the potential of stall margin improvement.

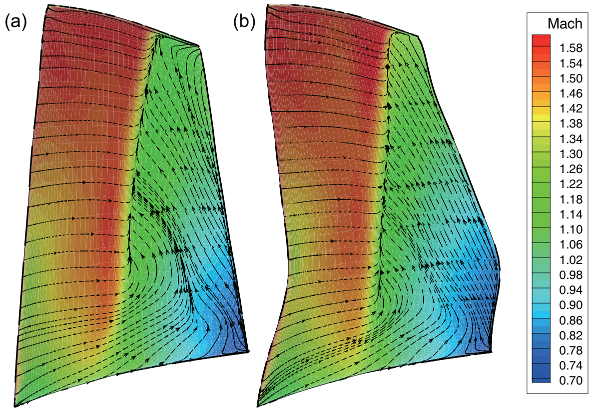

Figure 14 (Color online) Contours of isentropic relative Mach number near the suction surface. (a) Reference blade; (b) optimized blade.

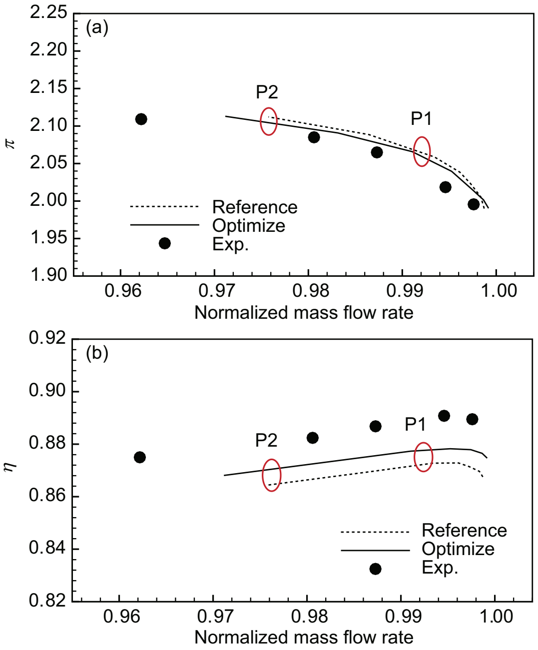

Figure 15 (Color online) Operation characteristics. (a) Total pressure ratio; (b) adiabatic efficiency.

5.3 Optimization of a single stage

5.3.1 Model validation

The redesign of the single compressor stage strives to reduce the flow separation zones in the stator passage. The stagger angle of the stator blade along the span was changed to adjust to the incident flow. Four control points on 0%, 40%, 80%, and 100% spans were perturbed. The perturbations at 40% span and 80% span were identical to achieve a uniform stagger angle change on these spans. In such situations, there are essentially three control points. With a given input of stagger angle change on the three spans, the determination of spanwise distribution of stagger angle change and the configuration of the sample stator blade are similar to the inverse design case of Section 5.1. Once the flow solutions were obtained, the spanwise distributions of stagger angle change of the last stator blade and the outlet flow were regarded as one POD snapshot.

A group of 3^3=27 uniform samples were generated for testing and another group of 21 initial LHD samples were generated by the multi-objective optimization. The adiabatic efficiency and mass-averaged flow turning of the stage at the operation condition near stall were regarded as cost function and optimization constraint, respectively. The average deviation tolerance was 0.01. By the ALHD method, two groups of 65 and 89 samples were necessary to construct the POD-QPRS and POD-RBF hybrid models, respectively, with satisfied response accuracy. Table 5 lists the sample numbers and average deviations. Similarly, the function response on adiabatic efficiency converged slower than that of the flow turning. As in the previous two optimization cases, the response performance of the POD-RBF model was better than that of the POD-QPRS model. In the flow reconstructions of the low-speed subsonic compressor stage, the response performance of the POD-QPRS model was better.

Figure 17 presents the pressure contours on the stage outlet plane for two test samples with maximum and minimum deviations, where the POD solutions were obtained from the POD-QPRS model. It can be seen that for the test sample with minimum deviation, the POD solution was almost a duplicate of the CFD solution, while there were visible differences between the POD and CFD solutions for the test sample with maximum deviation. However, through mass-averaging on the outlet plane, the POD-based and CFD-based flow solutions were very similar.

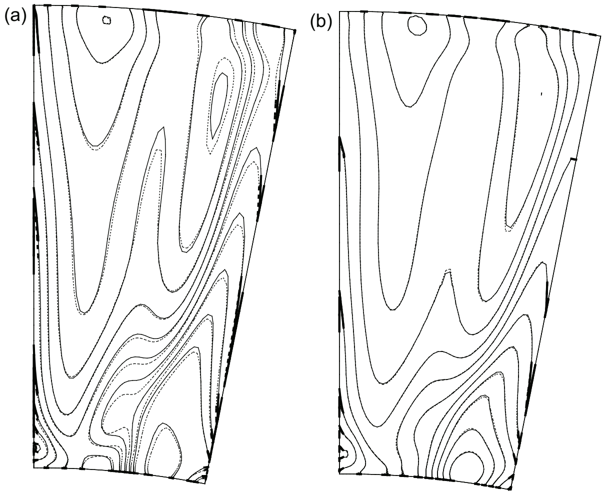

Figure 17 CFD and POD pressure contours at the stage outlet. (a) Maximum deviation; (b) minimum deviation. Dash line–POD; solid line–CFD.

For the low-speed single compressor stage, the POD-QPRS model performed better than the POD-RBF model on flow reconstructions, which was quite different from the previous two reconstruction studies. The most intensive flow characteristic of this stage was the flow separation in the stator passage. However, it is well known that the flow separation can be reduced by decreasing the incidence angle. In other words, the nonlinear dependence of flow separation on stagger angle change is weak. Furthermore, because of the effects of numerical dissipation, flow diffusion, and flow mixing, the characteristic of flow separation cannot be so intensive at the stage outlet. As shown in Figure 17, in blue the outlet pressure contours for two different samples were very close. As previously mentioned, the response performance of the RBF model is excellent for strong nonlinear problems. In this case, the weak nonlinear dependence of outlet flow on stagger angle change is suggested to be the most important reason for the better response performance of the POD-QPRS model. The group of ALHD samples used for constructing the POD-QPRS hybrid model were used in the following design optimization.

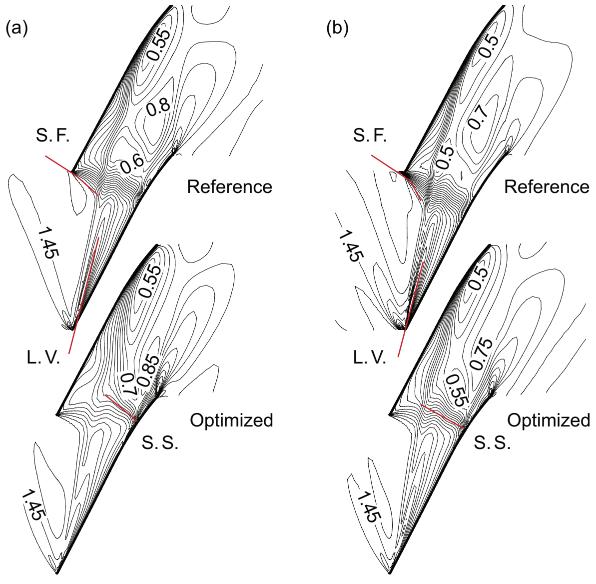

Figure 16 (Color online) Contours of relative Mach number on the blade-to-blade streamsurface at the blade tip. (a) P1; (b) P2.

Table 5 Sample numbers and average deviations

Model	n	$\bar{\epsilon}_\eta$	$\bar{\epsilon}_\beta$
POD-QPRS	65	9.07×10^{-3}	3.81×10^{-3}
POD-RBF	89	9.49×10^{-3}	4.16×10^{-3}

5.3.2 Optimization design

The spanwise stagger angle change of each GA individual was determined by eq. (15). The circumferentially mass-averaged adiabatic efficiency and flow turning along the span regarded as the missing subvectors was reconstructed by the POD-QPRS model. The overall aerodynamic performance was determined at the stage outlet. Then, the cost function given by eq. (12) was calculated. The outlet flow turning was regarded as the only constraint with the change tolerance $\epsilon_3 = 0.5\%$.

After optimization, a gain of 1.47% for adiabatic efficiency was obtained. The deviation of flow turning was about 0.41%. The optimal stagger angle change along the span is given in Figure 18. From the hub to about 40% span and from 80% span to the blade tip, the redesign performed a positive stagger change, while it performed a negative change from

40% to 80% span. The positive stagger angle change near the endwalls effectively reduced the incidence angle of the stator blade, favoring the suppression of flow separation with increased flow turning. The negative stagger angle change on the middle spans resulted in decreased flow turning.

Figure 19 presents the Mach number contours on the blade-to-blade streamsurface at about 10% span. Figure 20 presents the streamlines and the Mach number contours near the suction surface. The results demonstrate that the flow separation zones near the hub and casing of the optimized stator were significantly reduced.

Figure 21 presents the spanwise distributions of aerodynamic parameters for the reference and optimized stator blades, where ξ and ψ denote the flow loss and flow uniformity, respectively, the definitions of which are

$$\xi_{r\theta} = \frac{(p_{\mathrm{s},r\theta}/p_{\mathrm{t2},r\theta})^{(\gamma-1)/\gamma} - (p_{s,r\theta}/p_{\mathrm{t1},r\theta})^{(\gamma-1)/\gamma}}{1-(\bar{p}_{\mathrm{s,MS}}/\bar{p}_{\mathrm{t1,MS}})^{(\gamma-1)/\gamma}}, \tag{22}$$

$$\psi = \frac{1}{2}\int_r\int_\theta (q_{r\theta}-\bar{q}_r)^2 \mathrm{d}\theta \mathrm{d}r, \tag{23}$$

where the subscripts "s", "t1" and "t2" denote the static pressure, the total pressure at inlet and outlet, respectively, "MS" denotes the middle span at the inlet, q is the absolute velocity, and $\bar{q}_r$ denotes the circumferentially mass-averaged absolute velocity at span r.

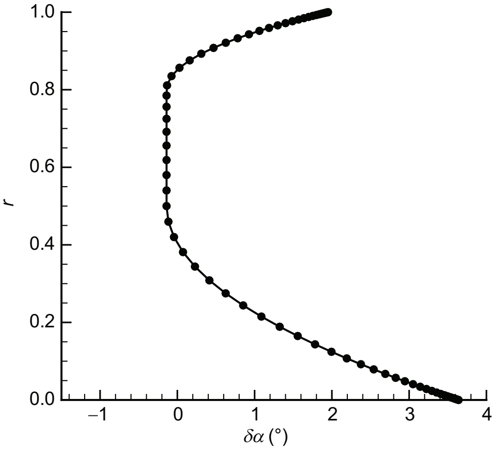

Figure 18 Spanwise distribution of stagger angle change.

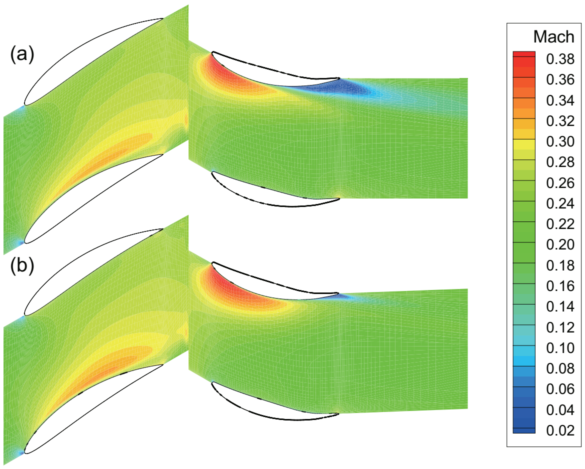

Figure 19 (Color online) Mach number contours on the blade-to-blade streamsurface at about 10% span. (a) Reference; (b) optimization.

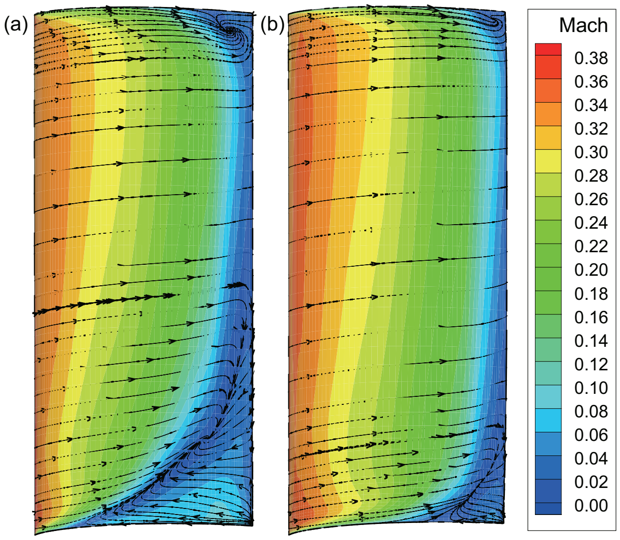

Figure 20 (Color online) Mach number contours near the suction surface. (a) Reference; (b) optimization.

It can be seen from Figure 21 that the flow loss near the hub decreased significantly after optimization, while the adiabatic efficiency on the entire span increased. The improvements of flow uniformity around the hub and casing are evident because of the reduced flow separation zones near the endwalls. The flow turning increased on the spans where the stagger angle performed positive changes, whereas it decreased on the middle spans. In such situations, the flow turning constraint was enforced.

The optimization was performed at the operation condition near stall of the 4.5-stage compressor. The performance improvements of the last stage in the entire operation range through the redesign of the stator blade are illustrated in Figure 22, where the total pressure ratio and adiabatic efficiency of the rotor and the stage are given and compared. The total pressure ratio of the stage increased slightly in a narrow operation range, while that of the rotor was almost unchanged because the aerodynamic shape of the rotor blade was maintained in the design optimization and therefore the operation condition of the rotor could not be changed significantly. In such cases, improvements on the adiabatic efficiency of the rotor were also invisible. However, the adiabatic efficiency of the stage increased in a wide operation range. At the operation conditions beyond 105% designed mass flow rate, the

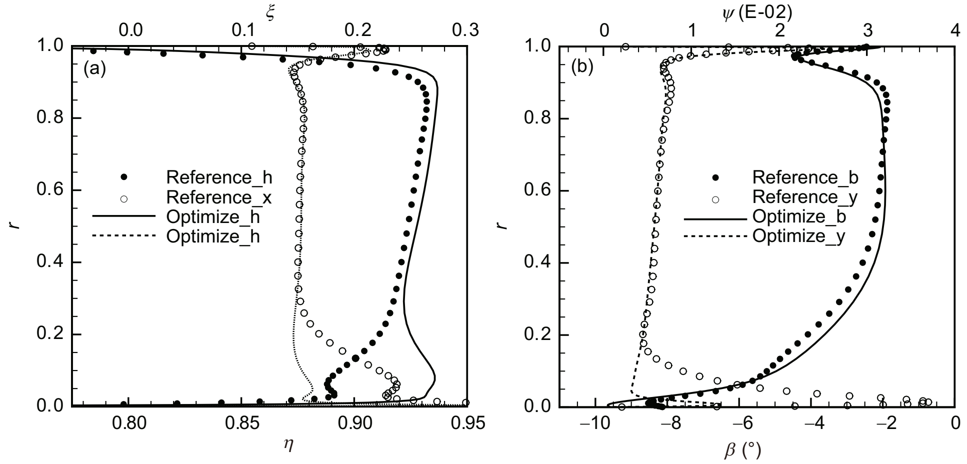

Figure 21 Spanwise distributions. (a) Adiabatic efficiency and flow loss; (b) flow turning and flow uniformity.

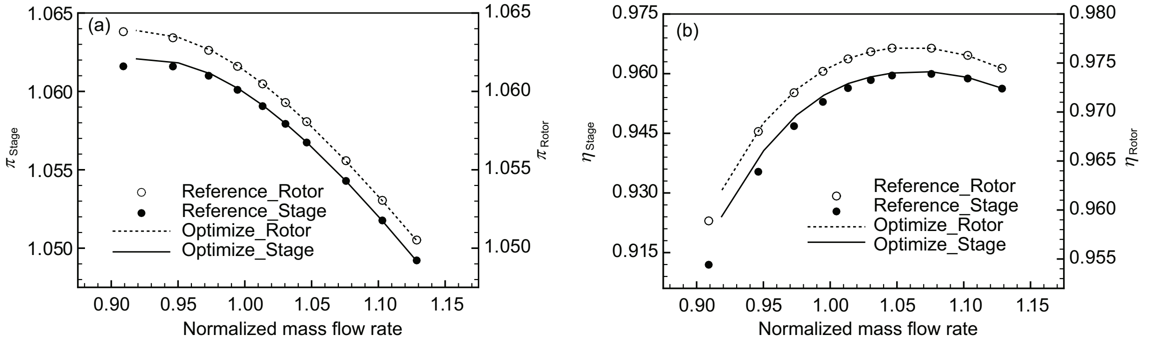

Figure 22 Operation characteristics. (a) Total pressure ratio; (b) adiabatic efficiency.

improvements on adiabatic efficiency were also invisible because, as the back pressure decreased, the flow separation zones in the stator passage decreased and even vanished with a low back pressure. In such situations, the flow loss induced by flow separation and improvements were consequently reduced.

6 Conclusions

This study presented a hybrid model method based on POD, in particular, the constructions of POD-based hybrid models by the means of nonlinear regressions to respond the coefficients of POD basis modes and an ALHD method based on a multi-objective optimization approach. Then, the hybrid models were used for flow reconstructions of a supersonic turbine blade, a transonic compressor rotor, and a single compressor stage. The response performance of the models was validated in each optimization case and then applied to the blade redesign. The results of flow reconstructions and the POD-based design optimization demonstrated that as followed.

(1) By the multi-objective optimization approach, a group of samples with the lowest average correlation and the maximin Euclidean distance can be picked up in the system space starting from a sequential permutation. Compared to an OLHD, although the average correlation cannot be exactly zero, the sample number no longer depends on the input number.

(2) Using an ALHD, additional samples were added into the target subspace where the response deviation was a maximum in the current LHD cycle. In such situations, the function response of each test sample was taken into account for the model construction. The number of ALHD samples can be significantly reduced compared with the static LHD.

(3) For different kinds of flow reconstructions, the function responses by the QPRS and RBF models performed differently. For the linear or quasi-linear problems, the response accuracy of the POD-QPRS model was better, whereas the POD-RBF model performed better for strong nonlinear problems.

Through the inverse design of stagger angle change along the span, the effectiveness of POD-based design optimization was validated. By changing the spanwise sweep of a transonic rotor blade and the spanwise stagger angle of the stator blade of a single compressor stage, the aerodynamic performance was significantly improved, while the optimization constraints of mass flow rate, total pressure ratio, and flow turning were maintained. The results demonstrate that the POD-based hybrid models are a powerful tool for not only flow reconstructions with sufficient description accuracy but also for aerodynamic design optimization in aerospace engineering.

This work was supported by the National Natural Science Foundation of China (Grant Nos. 51676003, 51206003 and 51376009). The authors would like to thank Dr. ZHAN Lei of Peking University for his help of the paper.

1 Couplet M, Sagaut P, Basdevant C. Intermodal energy transfers in a proper orthogonal decomposition Galerkin representation of a turbulent separated flow. J Fluid Mech, 2003, 491: 275–284

2 Couplet M, Basdevant C, Sagaut P. Calibrated reduced-order POD-Galerkin system for fluid flow modelling. J Comp Phys, 2005, 207: 192–220

3 LeGresley P A, Alonso J J. Investigation of non-linear projection for POD based reduced order models for aerodynamics. AIAA Paper 2001-0926, 2001

4 Willcox K, Peraire J. Balanced model reduction via the proper orthogonal decomposition. AIAA J, 2002, 40: 2323–2330

5 Dowell E, Hall K, Thomas J, et al. Reduced order models in unsteady aerodynamics. AIAA Paper 99-1261, 1999

6 Pathak K, Yamaleev N K. POD-based reduced-order model for arbitrary Mach number flows. AIAA Paper 2011-3111, 2011

7 Sirovich L, Kirby M. Turbulence and the dynamics of coherent structures. Part I: Coherent structures. Quart Appl Math, 1987, 45: 561–571

8 Luo J, Duan Y, Tang X, et al. An iterative inverse design method of turbomachinery blades by using proper orthogonal decomposition. ASME Paper GT2015-42876, 2015

9 Everson R, Sirovich L. Karhunen-Loeve procedure for Gappy POD. J Opt Soc Am A, 1995, 12: 1657–1664

10 Bui-Thanh T, Damodaran M, Willcox K E. Aerodynamic data reconstruction and inverse design using proper orthogonal decomposition. AIAA J, 2004, 42: 1063–1070

11 LeGresley P A, Alonso J J. Airfoil design optimization using reduced order models based on proper orthogonal decomposition. AIAA Paper 2000-2545, 2000

12 Duan Y, Cai J, Li Y. Gappy proper orthogonal decomposition-based two-step optimization for airfoil design. AIAA J, 2012, 50: 968–971

13 Panzini G, Sciubba E, Zoli-Porroni A. An improved proper orthogonal decomposition technique for the solution of a 2-D rotor blade inverse design problem using the entropy generation rate as the objective function. ASME Paper IMECE2007-43461, 2007

14 Kato H, Funazaki K I. POD-driven adaptive sampling for efficient surrogate modeling and its application to supersonic turbine optimization. ASME Paper GT2014-27229, 2014

15 Luo J, Duan Y, Xia Z. Transonic flow reconstruction by an adaptive proper orthogonal decomposition hybrid model (in Chinese). Acta Phys Sin, 2016, 65: 124702

16 Braconnier T, Ferrier M, Jouhaud J C, et al. Towards an adaptive POD/SVD surrogate model for aeronautic design. Comp Fluids, 2011, 40: 195–209

17 Guenot M, Lepot I, Sainvitu C, et al. Adaptive sampling strategies for non-intrusive POD-based surrogates. Eng Comput, 2013, 30: 521–547

18 Zhou G, Duan L B, Zhao W Z, et al. An enhanced hybrid and adaptive meta-model based global optimization algorithm for engineering optimization problems. Sci China Tech Sci, 2016, 59: 1147–1155

19 Finkel R A, Bentley J L. Quad trees: A data structure for retrieval on composite keys. Acta Inform, 1974, 4: 1–9

20 Mckay M D, Beckman R J, Conover W J. A comparison of three methods for selecting values of input variables in the analysis of output from a computer code. Technometrics, 2000, 42: 55–61

21 Tang B. Selecting Latin hypercubes using correlation criteria. Stat Sin, 1998, 8: 965–977

22 Ye K Q. Orthogonal column Latin hypercubes and their application in computer experiments. J Am Stat Assoc, 1998, 93: 1430–1439

23 Ye K Q, Li W, Sudjianto A. Algorithmic construction of optimal symmetric Latin hypercube designs. J Stat Plan Infer, 2000, 90: 145–159

24 Jin R, Chen W, Sudjianto A. An efficient algorithm for constructing optimal design of computer experiments. J Stat Plan Infer, 2005, 134: 268–287

25 Joseph V R, Hung Y. Orthogonal-maximin Latin hypercube designs. Stat Sin, 2008, 18: 171–186

26 Jordan M I, Jacobs R A. Hierarchical mixtures of experts and the EM algorithm. Neural Comput, 1994, 6: 181–214

27 Denton J D. The 1993 IGTI scholar lecture: Loss mechanisms in turbomachines. J Turbomach, 1993, 115: 621–656

28 Reid L, Moore R D. Design and overall performance of four highly loaded, high-speed inlet stages for an advanced high-pressure-ratio core compressor. NASA TP 1337, 1978

29 Luo J, Xiong J, Liu F, et al. Three-dimensional aerodynamic design optimization of a turbine blade by using an adjoint method. J Turbomach, 2011, 133: 011026

30 Denton J D, Xu L. The effects of lean and sweep on transonic fan performance. ASME Paper GT2002-30327, 2002

31 Samad A, Kim K Y, Goel T, et al. Multiple surrogate modeling for axial compressor blade shape optimization. J Propul Power, 2008, 24: 301–310

32 Yang J, Luo J, Xiong J, et al. Aerodynamic design optimization of the last stage of a multi-stage compressor by using an adjoint method. ASEM Paper GT2016-56893, 2016

33 Liu F, Jameson A. Multigrid Navier-Stokes calculations for three-dimensional cascades. AIAA J, 1993, 31: 1785–1791

34 Zheng X Q, Liu F. Staggered upwind method for solving Navier-Stokes and k-omega turbulence model equations. AIAA J, 1995, 33: 991–998

35 Spalart P R, Allmaras S R. A one-equation turbulence model for aerodynamic flows. AIAA Paper 92-0439, 1992

36 Luo J, Zhou C, Liu F. Multipoint design optimization of a transonic compressor blade by using an adjoint method. J Turbomach, 2014, 136: 051005

37 Luo J, Liu F. Multi-objective optimization of a transonic compressor rotor by using an adjoint method. AIAA J, 2015, 53: 797–801

38 Luo J, Liu F, McBean I. Turbine blade row optimization through endwall contouring by an adjoint method. J Propul Power, 2015, 31: 505–518

39 Denton J D. The calculation of three-dimensional viscous flow through multistage turbomachines. J Turbomach, 1992, 114: 18–26

40 Chima R V. Calculation of multistage turbomachinery using steady characteristic boundary conditions. AIAA Paper 98-0968, 1998

41 Saxer A P, Giles M B. Predictions of three-dimensional steady and unsteady inviscid transonic stator/rotor interaction with inlet radial temperature nonuniformity. J Turbomach, 1994, 116: 347–357